

# 3D Resolved Computational Modeling to Simulate the Electrolyte Wetting of a Lithium-Ion Battery Cell with 18650 Format

Emmanuel Yerumoh, Imelda Cardenas-Sierra, Francisco Fernandez, and Alejandro A. Franco\*

Electrolyte wetting in a lithium-ion battery (LIB) cell is a time-intensive and quality-critical manufacturing step that determines the degree of homogeneity of lithium ion's transport within the electrode and separator pores, affecting the overall ionic conductivity and current density. If the electrolyte is inadequately distributed, it can compromise the cell performance. In this work, we introduce a novel engineering-oriented model to simulate electrolyte wetting in a  $\text{LiNi}_{0.33}\text{Mn}_{0.33}\text{Co}_{0.33}\text{O}_2$ -graphite 18650 cylindrical LIB cell. Governing equations are supported on a pressure-saturation formulation incorporating Darcy's law and phase-transport expressions, solved through the finite element method in COMSOL Multiphysics. The model is parameterized

with experimental data extracted from literature, and free parameters are optimized via a sensitivity analysis to maximize wetting. Results indicate that saturation is predominantly controlled by the capillary pressure and the spatial electrolyte distribution across the different functional layers of the jelly roll (electrodes and separator). The obtained electrolyte saturation of 86% is consistent with saturation values reported in literature obtained with different methodologies. Our 3D-resolved modeling approach uniquely captures how 18650 cell spiral geometry and component properties influence electrolyte distribution and, to the best of our knowledge, it is the first capable to simulate wetting behavior in a full-scale cylindrical LIB cell.

## 1. Introduction

Lithium-ion batteries (LIBs) are at the forefront of modern energy storage technology, enabling a wide range of applications from mobile phones to electric vehicles (EVs).<sup>[1]</sup> Although several alternative energy storage technologies are currently under development, there is still much potential to be exploited from LIB technology.<sup>[2,3]</sup> Demand for these technologies is expected to

continue to grow, based on projections from government and private institutions. Various research efforts are underway to improve their performance and lifespan, with a recent strong emphasis on the manufacturing process, triggered by the multiplication of LIB European Gigafactory initiatives and the need for them to get through the financial "valley of death". The LIB cell manufacturing process involves numerous intricate and critical stages, including slurry formulation, slurry mixing, coating and drying, electrode calendering, electrolyte filling and wetting, cell assembly, and solid electrolyte interphase formation.<sup>[4]</sup> Changes in the parameters of each one of these manufacturing steps have an impact on their further electrochemical performance evaluation. The electrolyte wetting step is a crucial stage in the production of LIB cells due to its impact on the cell performance, safety, and lifespan. This step is also generally considered to be time-consuming and quality critical.<sup>[5]</sup> Numerous experimental studies have been proposed to optimize the electrolyte filling/wetting step, mainly by utilizing vacuum and complex multistage pressure filling setups.<sup>[6,7]</sup> Computational modeling counterparts have also contributed to the understanding of the electrolyte infiltration dynamics at the micro- and macroscales.<sup>[7–10]</sup> However, several challenges still limit the effectiveness and efficiency of this step, mainly in achieving a uniform, homogeneous, and complete electrolyte distribution within the cell.<sup>[11]</sup> At the time of writing this article, industrial-scale electrolyte filling is being automated and performed with the use of high-precision equipment. This approach eliminates inconsistencies and increases the reproducibility of mass-produced LIB cells.<sup>[12]</sup> The filling is accomplished through a combination of steps in a multistage filling process where infiltration is performed under vacuum to ensure better

E. Yerumoh, I. Cardenas-Sierra, F. Fernandez, A. A. Franco  
Laboratoire de Réactivité et de Chimie des Solides (LRCS)  
UMR CNRS 7314

Université de Picardie Jules Verne, Hub de l'Energie  
15 rue Baudelocque, 80039 Amiens Cedex, France  
E-mail: alejandro.franco@u-picardie.fr

E. Yerumoh, I. Cardenas-Sierra, F. Fernandez, A. A. Franco  
Réseau sur le Stockage Electrochimique de l'Energie (RS2E)  
Fédération de Recherche CNRS 3459  
Hub de l'Energie  
15 rue Baudelocque, 80039 Amiens Cedex, France

A. A. Franco  
ALISTORE-European Research Institute  
Fédération de Recherche CNRS 3104  
Hub de l'Energie  
15 rue Baudelocque, 80039 Amiens Cedex, France

A. A. Franco  
Institut Universitaire de France  
103 Boulevard Saint Michel, 75005 Paris, France

 Supporting information for this article is available on the WWW under <https://doi.org/10.1002/batt.202500434>

 © 2025 The Author(s). *Batteries & Supercaps* published by Wiley-VCH GmbH. This is an open access article under the terms of the Creative Commons Attribution License, which permits use, distribution and reproduction in any medium, provided the original work is properly cited.

saturation and uniform distribution throughout the porous electrodes and separator.<sup>[13]</sup> Despite these advances in the filling process, issues such as entrapped air, incomplete saturation, and inconsistent wetting, remain as challenges to be solved.<sup>[12–14]</sup> Entrapped air and gases are detrimental because they can block the transport pathways of lithium ions, increasing the effective tortuosity factor and decreasing the effective ionic conductivity, as we have previously discussed in earlier works.<sup>[9,10]</sup> This inhomogeneous electrolyte distribution affects the concentration of lithium ions, resulting in non-uniform current densities and an increased risk of lithium plating.<sup>[13–16]</sup> Trapped gases can also create zones where the active material (AM) surface is not in contact with the electrolyte, which contributes to a reduced electrochemical performance and eventually leads to aging.<sup>[9]</sup> Additional challenges can also be introduced during the previous manufacturing steps, such as the calendering stage, which consists of pressing the electrodes to increase their energy density and electronic conductivity.<sup>[17]</sup> This step is crucial as it determines the final porous network and the electrochemical performance.<sup>[18]</sup> However, calendering results in lower electrode porosities and permeabilities, which translates into slower wetting rates and longer electrolyte saturation time during the filling step.<sup>[9,19]</sup> Depending on the geometry, size, and format of the cell, optimal electrolyte infiltration can take from a few minutes (for laboratory coin or pouch cells) to a few hours, or even several days (for commercial cylindrical or prismatic cells).<sup>[20–23]</sup> In addition, it is a common practice in the industry to use elevated temperatures and overestimate the wetting time to ensure maximum wetting.<sup>[24]</sup> Indeed, optimization of the electrolyte filling and wetting process is considered to improve the performance of the cells.

Various experimental techniques have been used in the past to characterize the electrolyte wetting process.<sup>[25–29]</sup> These approaches are usually time-consuming and expensive, as they rely on an iterative experimental approach to find the optimal wetting conditions. For this reason, and to speed up the understanding and optimization of this critical manufacturing step, experimental work can be complemented with computational modeling simulations. The use of this digital approach has increased in recent years and has already been applied to other stages of the manufacturing process, in particular by our group.<sup>[30–32]</sup> Modeling is a valuable tool for predicting results and optimizing production parameters to achieve specific target properties for different applications. When these approaches are used together, they can improve experimental design and optimize parameters and performance. In the LIB cell manufacturing process, the mesoscale models of our ARTISTIC research initiative<sup>[30]</sup> have demonstrated that computational modeling can accelerate the understanding of the relationships between the cell performance and the manufacturing parameters.<sup>[33]</sup> Various types of models have been used to simulate and predict electrolyte wetting properties.<sup>[7,23,34]</sup> These models have focused on simulating 1D and 2D cell geometries,<sup>[5,34]</sup> which provide many valuable insights, but are often limited in capturing the full complexity of the process, and have limited wetting mechanism accuracy due to their reduced order geometry.

Recent advances in computational modeling have resulted in more sophisticated 3D models that provide a more realistic representation of the infiltration process.<sup>[7–10,14]</sup> Shodiev et al. from our group, pioneered the 3D-resolved simulation of wettability using the Lattice Boltzmann Method (LBM) in LIB electrodes. These LBM simulations were carried out with electrode microstructures arising from computer tomography characterization and from meso-scale manufacturing simulations using coarse-grained molecular dynamics and the discrete element method.<sup>[9]</sup> The model showed that the degree of electrolyte penetration is influenced by the microstructural features of the electrode, such as its pore size distribution, tortuosity factor, and porosity. Electrolyte penetration was also found to depend on various electrolyte features, such as its viscosity, its density, or its contact angle with the electrode. This model was also used to simulate electrolyte infiltration in cell sandwiches consisting of electrodes with gradients of porosity and AM particle sizes along their thickness.<sup>[10]</sup> It was found that the presence of these gradients helped accelerate the electrolyte wetting dynamics in the electrodes and in the separator. Then, Lautenschlaeger et al. used a LBM model to simulate the electrolyte filling process in artificially generated electrodes,<sup>[14]</sup> where a two-phase flow of electrolyte and gas was considered as in the model of Shodiev et al. These electrodes were generated using a force-biased sphere-packing algorithm to randomly allocate AM particles based on a Gamma distribution. The particles were reshaped using a spherical harmonics-based method to reflect realistic morphologies. However, no direct link to manufacturing parameters was established during the electrode microstructure generation. In addition, Wanner et al. proposed a similar LBM model for the wetting step of the battery cell anode and separator.<sup>[8]</sup> Based on their laser scanning microscopy data, they stochastically generated 3D microstructures containing fixed-radius AM spherical particles that could sporadically touch each other. They studied the influence of porosity and pore size on the wetting behavior.<sup>[8]</sup> To improve the visualization of the wetting processes, Wanner et al.<sup>[35]</sup> used a glass cell housing for a 21700 cylindrical cell at different temperatures and pressures, and studied the influence of these parameters using an LBM pore-scale simulation. They found that electrolyte wetting has a strong dependence on temperature and pressure changes. They reported that a heterogeneous distribution of electrolyte after filling leads to gas entrapment. However, one of the limitations of this approach is that the electrolyte movements in the inner windings cannot be observed, due to the limited resolution through the glass cell. The above models usually fail to provide such type of insights at the cell scale. Furthermore, increasing the scale of such models to account for an entire cell configuration would be highly computationally expensive. 3D LBM models are typically used to simulate small portions of the electrode and the cell, with volumes in the order of some dozens of microns in each direction. This limits their use for macroscale simulation of the infiltration and wetting processes of a battery cell, especially those with complex macroscopic geometries. Numerical 2D and 3D continuum models using computational fluid dynamics (CFD) were also used to provide insights at the cell scale by studying the electrolyte filling and wetting processes for the full LIB

cells.<sup>[7]</sup> Using the specifications of a standard plug-in hybrid EV cell format and images from an X-ray microcomputer tomography analysis of a  $\text{Li}_{x}\text{Ni}_{0.33}\text{Mn}_{0.33}\text{Co}_{0.33}\text{O}_2$  (NMC111) cathode, Hagemeister et al. developed a model to study the effects of pressure and temperature during the filling process.<sup>[7]</sup> They applied the established filling model to study the effects of evacuation pressure and temperature during the electrolyte filling process at the cell scale, experimentally validating it for both hardcase and pouch cells. They estimated porosity and permeability with a CFD microsimulation of an anode, and a cathode porous microstructure used to obtain the capillary-driven wetting rate.<sup>[36]</sup> Dent et al. developed a continuum-level volume averaged model to simulate electrolyte impregnation, dynamics of ion transport, and electrochemical processes in a LIB 26650 cylindrical cell with LFP-Graphite chemistry and a laboratory coin cell with Li-S chemistry.<sup>[23]</sup> They focused their study on a small representative section of the cell considering adjacent anode, cathode, and separator layers. They also considered a three-phase system with solid, void, and liquid electrolyte phases, which they characterized by saturation and pore size distribution. Particularly, for the Li-S case, they considered the dissolution and precipitation of species. Their simulation for a cylindrical LIB cell predicted an impregnation time of 7 days, considering the cell in rest and going from homogeneous electrolyte distribution up to the micropores.<sup>[23]</sup>

Currently, there is a lack of computational models that allow the optimization of the wetting process by analyzing the impact of the macroscale heterogeneities for complex LIB cell geometries, such as the tightly packed jelly roll of the 18650 cylindrical format. Specifically, a computational approach that allows the use of volume-averaged properties of domains and could help to develop this type of model is the finite element method (FEM). This method allows us, in the present work, to develop a model with an intermediate level of detail, where we are able to study the electrolyte wetting layer-by-layer and the complexity it induces. This approach contrasts with previously reported LBM models, resolving electrolyte wetting at the mesoscale, and macroscopic models, considering electrolyte wetting in a small representation of the whole cell geometry.

In this work, we propose novel 2D and 3D-resolved FEM models that allow simulating the electrolyte wetting process of a commercial NMC-graphite cell with 18650 cylindrical format, taking into account the real size and shape of the jelly roll. We reach a deeper understanding of the electrolyte wetting of this types of cells by explicitly considering the complex macroscale heterogeneities of the cell geometry, related to the placement and properties of the electrodes, the separators and the current collectors, the dynamics of the fluid flow in the porous media, and the boundary conditions. To implement the FEM models and perform our study, we used COMSOL Multiphysics,<sup>[37]</sup> a software widely used in the battery industry. Our article is organized as follows. First, we present the mathematical formulation behind our models, their subsequent parameterization, and the numerical details to solve them. Then, we present and discuss the results obtained by considering both 2D- and 3D-resolved model geometries. Finally, we conclude and give perspectives on the future of our research.

## 2. Computational Methods

The modeling framework presented here involves several key steps, as shown in Figure 1. The first step is to generate a virtual representation of the real cell geometry. In this case, the computer-aided design program SolidWorks was used.<sup>[38]</sup> We started with a 3D geometry design which was simplified into a 2D version. Once the electrolyte filling model was parameterized and demonstrated to work in 2D, we move back to 3D (Figure 1a). This consideration of a lower dimensionality for the cell geometry is a simplification of the problem and allows us to accelerate the testing of different parameters and how they affect the output properties. In the next step, the geometry is meshed using different sized mesh elements to find the best trade-off between resolution and computational cost (Figure 1b). The third step is to continue building the model by using a mathematical formulation of the CFD approach to simulate the electrolyte wetting through the cell. In this case, we consider a pressure-saturation formulation and Darcy's law (Figure 1c), which will be introduced in Section 2.2. Then, an averaged property approach is used to consider the different parameters of the model in the porous media. To parameterize the model (Figure 1d), the porous media are described by two fundamental properties, permeability and porosity, without considering a detailed description of the porous microstructures. Other external parameters, like the capillary pressure (Capillary P. in the figure) and the residual saturation (R. saturation in the figure), are also considered. This approach significantly reduces the computational cost when compared to more detailed techniques and allows the simulation of real-sized LIB cells. The final steps correspond to analysis and validation of the results against physical intuition and experimental data (Figure 1e,f).

The modeled system was a LIB cell in the 18650 cylindrical format, consisting of an NMC111 cathode and a graphite anode, with a Celgard 2500 separator. To reduce the computational cost, we focus first on building an accurate 3D representation of the jelly roll inside the casing. Other components were neglected due to their non-interference in the electrolyte wetting process. The flattened jelly roll consists of eight consecutive stacked layers which are rolled into a spiral of 21 turns (these values correspond to the typical number of layers found in real cells with 18650 format<sup>[39]</sup>). In this particular cell format, the eight layers consist of a double-sided anode, two separator layers, a double-sided cathode, and two current collectors.

An 18650 cylindrical format LIB cell showing the full jelly roll is presented in Figure 2a. The cross section of jelly roll is shown in Figure 2b, and a zoomed-in view highlighting the electrodes and separator layers is provided in Figure 2c. The FEM is used to solve the equations governing the electrolyte wetting into the LIB cell. This is accomplished by discretizing the geometry into small mesh elements and then calculating the solution on each one of these elements. Decreasing the mesh element size makes the solution more accurate. However, this also increases the computational cost. In this work, we considered different number of mesh elements for each model: 36159 for the 2D model, 24375370 for the 3D miniature spiral cell, and 5 million for the 3D

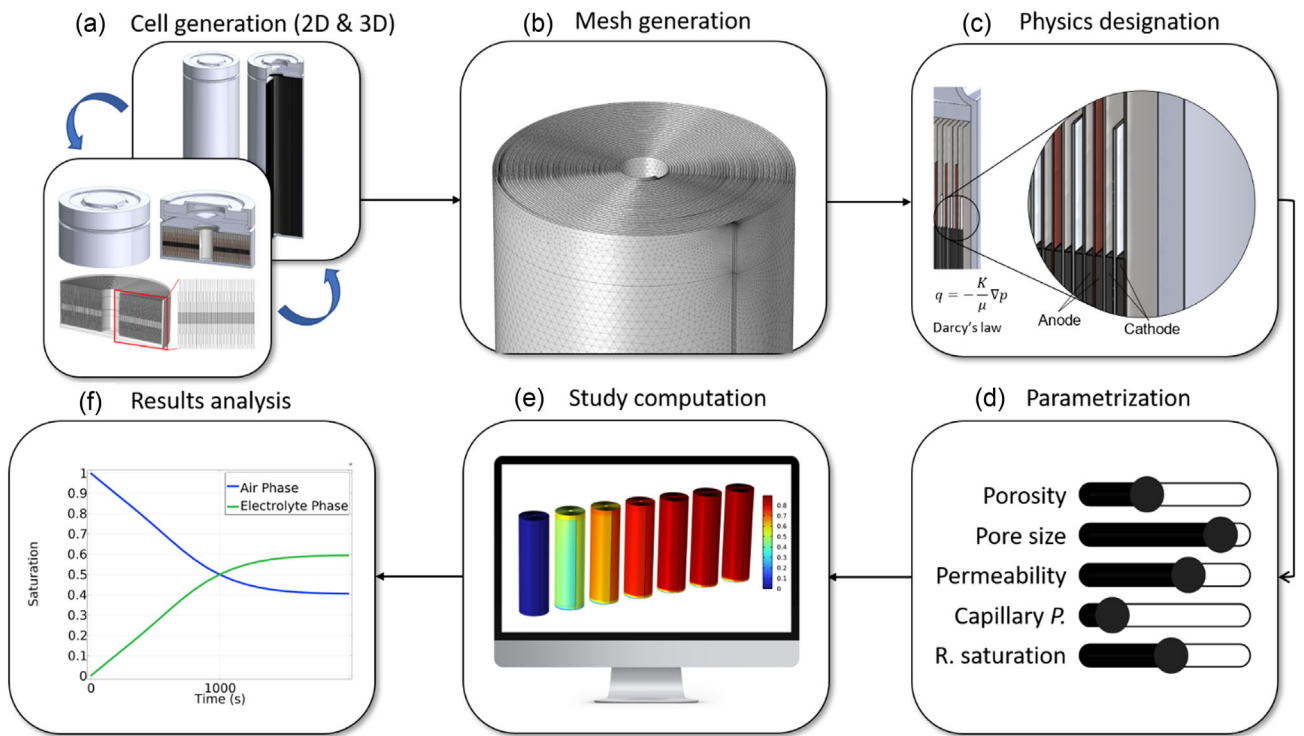


**Figure 1.** Computational modeling workflow, showing the successive steps adopted: a) cell geometry generation, b) mesh generation, c) physics designation, d) model parameterization, e) study computation, and f) results analysis.

spiral cell (full size), respectively (the definitions of the different types of models are provided below and in **Figure 3**). Also, the size of these mesh elements ranged from  $6.41 \times 10^{-4}$  to  $9.9 \times 10^{-7}$  m. These numbers of mesh elements and their size were chosen in order to optimize the trade-off between accuracy and computational cost.

The boundary conditions in the model are defined by selected values of pressure, saturation, and mass flux as indicated in **Table 1**. The location of these boundaries on the 3D geometry is illustrated in Figure 2d,e. The current collector boundaries are defined to apply a no-slip condition. In addition, a boundary condition to the flow velocity of the electrolyte is applied to the surface of the NMC111 cathode, the graphite anode, and the Celgard separator (see the second row of Table 1). A pressure boundary condition is also applied to the same locations. To specify the initial conditions for the saturation (volume fraction) of each phase, an initial state is considered in which the entire system is filled with air before the electrolyte starts the wetting process.

Due to the high computational cost of building an electrolyte wetting model using a 3D geometry representing a realistic (full size) 18650-format cell, we approach the problem by building a simplified 3D cell height (representing 2% of the height of the real 3D cell size, and hereafter referred to as miniature 3D cell). This new model is simplified further to a 2D model. This approach significantly reduces the computational cost and allows to perform faster preliminary parameter sensitivity analysis (taking only 5 min to run a simulation on the 2D model). Then, we come back to the 3D geometries (of both 3D miniature and 3D full size

models) and use the 2D model optimized parameters as a starting point. **Figure 3** shows the workflow for this modeling strategy.

The thicknesses of each component of the modeled LIB cell are given in **Table 2**. An electrolyte consisting of a 1M LiPF<sub>6</sub> solution in a 1:1 mixture of ethylene carbonate and diethyl carbonate is considered in both 2D and 3D models. All the simulations were performed at a reference temperature of 25 °C.

## 2.1. Formulation of the Electrolyte Wetting Model

The electrolyte infiltration process in a cell can be divided into two flow regimes: the pressure-driven flow (filling) and the capillary-driven flow (wetting). The first one is an ultrafast process that occurs in few seconds, when the filling process begins. This regime occurs mainly in the macroscopic regions, where the electrolyte fills the spaces present in the enclosure (between the porous electrodes/separator and the cell casing). The second regime is a prolonged process that lasts several hours, and it takes place inside the micropores of the porous media. This electrolyte flow is due to the pressure difference between the trapped air in the pores and the surrounding electrolyte, after the macroscopic pores are already saturated with electrolyte.

To simplify the computational complexity of the model, we focus on the capillary-driven flow (wetting) regime by assuming that the filling stage is already completed. We consider the two-phase flow of two incompressible fluids: electrolyte (wetting phase) and air (nonwetting phase), flowing through the porous parts of the jelly roll (electrodes and separator). The conservation

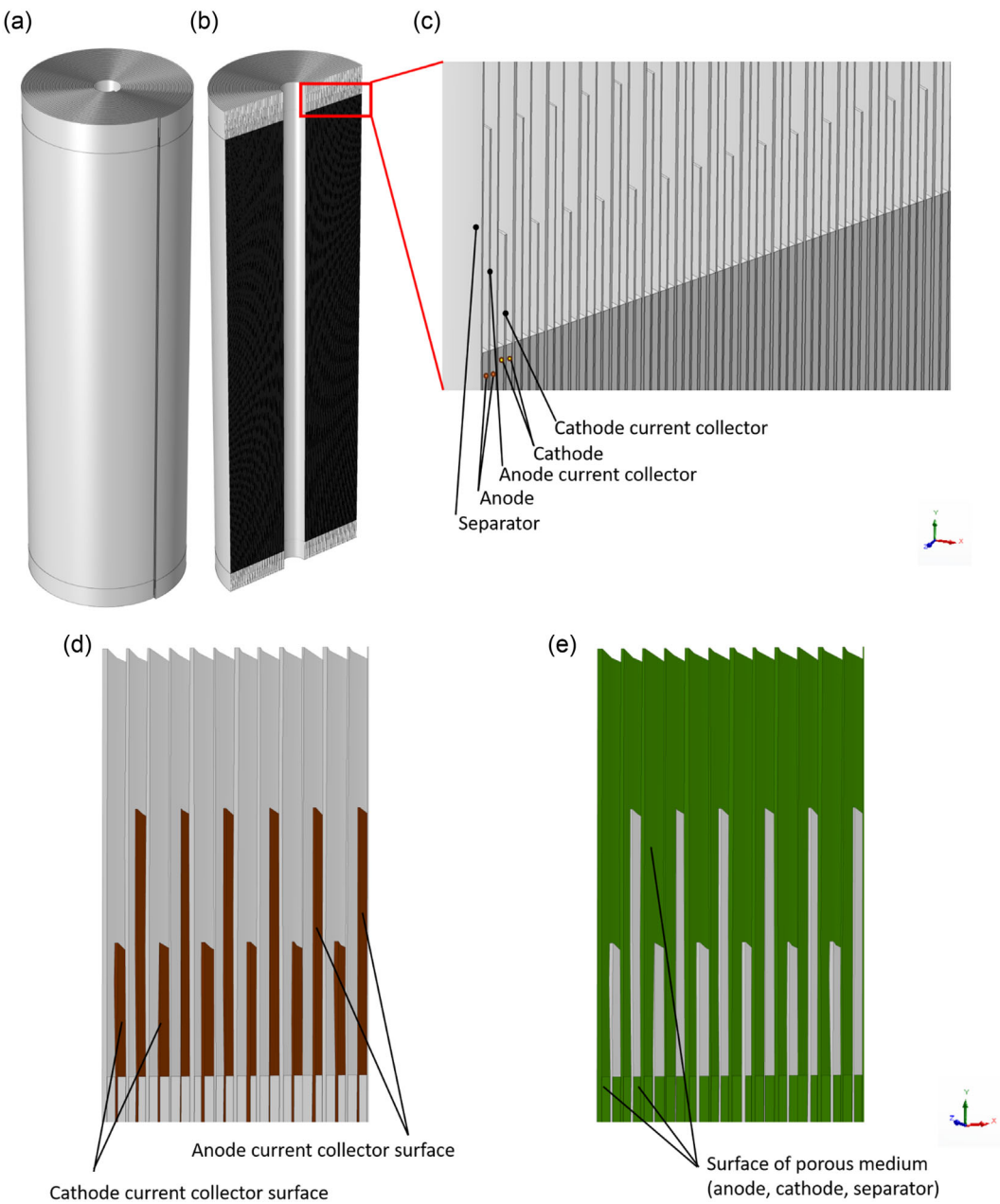


**Figure 2.** A cross-sectional view of the 18650 cell and the surfaces where the boundary conditions are applied. a) cell; b) cross-sectional view; c) zoomed-in view of the successive layers inside the jelly roll; d) cell geometry with surface of current collectors (highlighted in red); and e) cell geometry with surface of porous domains, positive and negative electrodes, and separators (highlighted in green).

of momentum for both phases is described by the Navier–Stokes equation,<sup>[40]</sup> which is given in vector form for incompressible fluids as follows

$$\frac{\partial(\rho\vec{u})}{\partial t} + \nabla \cdot (\rho\vec{u}\vec{u}) = -\nabla p + \mu\nabla^2\vec{u} + \vec{F} \quad (1)$$

where  $\vec{u}$  is the flow velocity ( $\text{m s}^{-1}$ ),  $\rho$  is the density ( $\text{kg m}^{-3}$ ),  $p$  is the fluid pressure (Pa),  $\mu$  is the fluid viscosity (Pa s), and  $\vec{F}$  the body force due to gravity (N). During the infiltration process, when the air is evacuated, the electrolyte mass is conserved and can be described by the continuity equation

$$\frac{\partial p}{\partial t} + \nabla \cdot (\rho\vec{u}) = 0 \quad (2)$$

When viscous forces dominate over inertia forces in a porous medium,<sup>[41]</sup> i.e., when the fluid flow is slow, the Darcy's law can be derived from the Navier–Stokes equation,

$$\vec{u} = -\frac{K}{\mu}(\nabla p - \rho g) \quad (3)$$

where  $K$  is the permeability of the porous medium ( $\text{m}^3$ ),  $\nabla p$  is the pressure gradient defined over a distance within the pores (Pa.m),

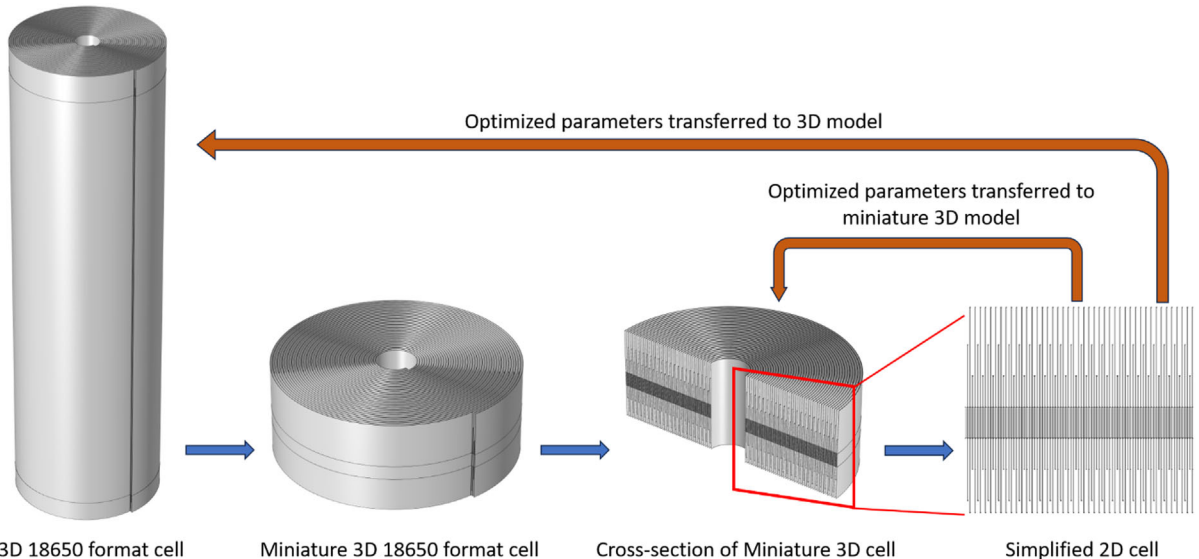


**Figure 3.** Scheme of the workflow of the adopted modeling strategy transitioning from the 3D geometry to the 2D model for optimizing the simulation parameters of the wetting process.

**Table 1.** Boundary and initial conditions applied on the 3D models.

Label in Figure 2	Boundary condition	
d	No flux	$\vec{u}(0) = 0$ $\vec{u}(t) = 0$
e	Mass flux	$\vec{u}(0) = (6.5, 6.5, 6.5) \times 10^{-6} \text{ kg (m}^2 \text{s)}^{-1}$ $\vec{u}(t) = (6.5, 6.5, 6.5) \times 10^{-6} \text{ kg (m}^2 \text{s)}^{-1}$
	Pressure	$P(0) = 800 \text{ kPa}$ $P(t) = 800 \text{ kPa}$

**Table 2.** Thicknesses of the cell components considered in the 2D and 3D models.

	Negative	Positive
Active material <sup>a)</sup>	Graphite	NMC111
Double-coated electrode thickness [μm]	126	125
Current collector foil thickness [μm]	10 (Cu)	20 (Al)
Separator thickness [μm]		16

<sup>a)</sup>The values correspond to double-coated electrodes typically found in 18650 cells.

and  $g (\text{m s}^{-2})$  denotes the acceleration due to gravity. Darcy's law is used to macroscopically describe the fluid flowing through porous media (in this case electrodes and separator) under pressure effects.

The conservation of mass, given by Equation (2), can be expressed for both the electrolyte and the air phases

$$\frac{\partial(\epsilon_j \rho_e s_e)}{\partial t} + \nabla \cdot (\rho_e \vec{u}_e) = 0 \quad (4)$$

$$\frac{\partial(\epsilon_j \rho_a s_a)}{\partial t} + \nabla \cdot (\rho_a \vec{u}_a) = 0 \quad (5)$$

where  $s_a$  is the saturation of air phase (i.e., the instantaneous fraction of porosity occupied by air) and  $s_e$  is the saturation of electrolyte phase and  $\epsilon_j$  is the porosity, where  $j$  refers to the porosities of the respective porous medium. In addition, a closure equation for the saturation is considered

$$s_e = 1 - s_a \quad (6)$$

With the Darcy's law (given in Equation (3)), we can solve  $\vec{u}_i$  (with  $i$  referring to electrolyte or air phase) for each phase, which gives the following flow velocity equations

$$\vec{u}_e = -\frac{K_{re}}{\mu_e} K (\nabla p_e - \rho_e g) \quad (7)$$

$$\vec{u}_a = -\frac{K_{ra}}{\mu_a} K (\nabla p_a - \rho_a g) \quad (8)$$

where  $K_{re}$  is the relative permeability of the electrolyte phase and  $K_{ra}$  is the relative permeability of the air phase. The phase pressures  $P_e$  (for the electrolyte phase) and  $P_a$  (for the air phase) are related through the capillary pressure  $P_c$  by the following equation

$$P_a - P_e = +P_c(1 - s_a) \quad (9)$$

Thus, the capillary pressure is necessary to solve each independently chosen phase pressure. The Brooks and Corey model was subsequently used to describe the capillary pressure<sup>[42]</sup>

$$P_c = P_{ec}(s_e^*)^{1/\lambda} \quad (10)$$

where  $s_e^*$  is the normalized saturation of the electrolyte phase (effective saturation) and  $P_{ec}$  is the entry capillary pressure of the electrolyte phase (pressure difference required to displace

the non-wetting fluid from the porous medium) and  $\lambda$  is the pore size distribution index (a parameter to be fitted).

The  $s_e^*$  is a quantity related to the residual saturation ( $s_r$ ) of each of the phases in the porous medium as it is given by the following equation

$$s_e^* = \frac{s_e - s_{re}}{1 - s_{ra} - s_{re}} \quad (11)$$

where  $s_{re}$  is the irreducible saturation of the electrolyte phase and  $s_{ra}$  is the irreducible saturation of the air phase. Equation (11) shows that the nonwetting phase cannot be completely displaced from the porous medium (some air remains trapped inside the electrode due to the clogged pores).<sup>[9]</sup> This is also true for the wetting phase. Therefore, we define this quantity as the residual saturation.

The Brooks and Corey model also defines the relative permeabilities of each phase as a function of saturation with the following equations

$$K_{re} = (s_e^*)^{\frac{2+3\lambda}{\lambda}} \quad (12)$$

$$K_{ra} = s_a^{*2} \left(1 - (1 - s_a^*)^{\frac{2+\lambda}{\lambda}}\right) \quad (13)$$

These equations analytically express the dependence of the relative permeabilities on the normalized saturations ( $s_e^*$  and  $s_a^*$ ) and the pore size distribution index.

With four unknown variables ( $P_e$ ,  $s_e$ ,  $P_a$ , and  $s_a$ ), we choose to use ( $P_e$ ,  $s_a$ ) as independent variables in the analytical formulation for the derivation of the remaining unknowns. Alternatively, a ( $P_a$ ,  $s_e$ ) analytical formulation could also be considered.<sup>[42]</sup>

To solve for the  $P_a$  or  $P_e$ , we make a straightforward substitution of the Equation (3), (7), and (8) into the mass balance Equation (4) and (5) for each phase, eliminating the direct dependence on the flow velocity, and resulting in the following two equations

$$\frac{\partial(\epsilon_p \rho_e (1 - s_a))}{\partial t} - \nabla \cdot \left( \rho_e \frac{K_{re}}{\mu_e} K (\nabla P_e - \rho_e g) \right) = 0 \quad (14)$$

$$\frac{\partial(\epsilon_p \rho_a s_a)}{\partial t} - \nabla \cdot \left( \rho_a \frac{K_{ra}}{\mu_a} K (\nabla P_e + \nabla P_c (1 - s_a) - \rho_a g) \right) = 0 \quad (15)$$

These two equations, expressed in terms of the electrolyte phase pressure and the saturation of the air phase, are the final set of equations used to calculate the pressures of the air and electrolyte phases.

## 2.2. Models Parameterization

The models were parameterized using data reported in the literature to represent real electrolyte wetting conditions (Table 3–5).

Table 3 shows the input parameters for each component of the LIB cell considered in this work. The porosity of the graphite and NMC111 electrodes, and of the separator, are experimental values extracted from a study done in our group by Shodiev et al.<sup>[9]</sup> The permeability and entry capillary pressure

**Table 3.** Input parameters for each component considered in our electrolyte wetting simulation models.

	Negative (graphite)	Positive (NMC111)	Separator (Celgard 2500)
Porosity [%]	31.50	25.00	55.00
Mean pore size [μm]	8.80	5.00	0.35
Permeability [m²]	$3.0492 \times 10^{-12}$	$7.8125 \times 10^{-13}$	$8.4230 \times 10^{-15}$
Residual saturation	0	0	0
Contact angle [°]	15	10	45
Entry capillary pressure [Pa]	6250.00	12000.00	128571.42

**Table 4.** Viscosity and density values for the electrolyte and air phases.

	Electrolyte	Air
Viscosity [Pa s]	$(4.7 \pm 0.1) \times 10^{-3}$	$1.81 \times 10^{-5}$
Density [ $\text{kg m}^{-3}$ ]	1300	1.18

**Table 5.** Boundary parameters for 3D resolved model.

Parameters	Physical value
Electrolyte impregnation pressure [kPa]	800
Mass flux [ $\text{kg m}^{-2} \text{s}^{-1}$ ]	$6.5 \times 10^{-6}$

of both electrodes and separator are calculated using empirical equations<sup>[43]</sup>

$$K = \frac{\epsilon r_{eff}^2}{8} \quad (16)$$

where  $r_{eff}$  is the median pore size and  $K$  is the permeability. The entry capillary pressure,  $P_{eC}$ , is given by

$$P_{eC} = \frac{2\gamma \cos\theta}{r} \quad (17)$$

In Equation (17),  $r$  is the pore radius,  $\theta$  is the contact angle between the porous layer and the electrolyte, and  $\gamma$  is the interfacial tension. Since the data for the entry capillary pressure values could not be found in the literature, the values given in Table 3 correspond to the final value obtained after optimization of the capillary pressure through a parametric study within a tolerable range. The range was identified by taking calculated capillary pressure values as a reference, which are estimated using  $\gamma_{EC/DEC} = 31 \text{ mN m}^{-1}$ <sup>[20]</sup> and assuming a low enough contact angle (from 0° to 30°).<sup>[20,44,45]</sup> Within this range, having a smaller contact angle results in a better electrolyte spreading on the surface of the electrodes. In particular, it has been demonstrated that lower contact angles indicate higher wettability.<sup>[44]</sup> For our particular case, the experimental values for the contact angles for the specific porous components and the electrolyte used, could not be found. In addition, assigning a different value of capillary pressure to each one of the porous components is not trivial, since the solver applies the highest entry pressure as a global

value. This led to an underestimation of electrolyte saturation degree in the electrodes. To better represent experimentally measured electrode saturations, we imposed the lowest capillary pressure (6250 Pa) on all domains. The trade-off of this consideration is that electrolyte infiltration in the separator occurs at a lower capillary pressure. For the full size 3D simulations we have further optimized the used capillary pressure as explained in Section 3.2.

As for the parameters of the electrolyte and the air located inside the cell, the values of the viscosity and the density are presented in Table 4. These values are taken from our previously reported studies.<sup>[9,46]</sup> For the electrolyte impregnation pressure, a typical industrial value is used, extracted from ref. [47]. The initial value for the mass flux of electrolyte through the micropores of the porous medium was estimated to be  $6.5 \times 10^{-6} \text{ kg m}^{-2} \text{ s}^{-1}$ . This value was obtained through a trial-and-error approach for the input pressure value and filling condition, starting from a reference value of  $0.03 \text{ kg s}^{-1}$ .<sup>[7]</sup> These two values are given in Table 5.

**Table 6** shows the capillary pressure-saturation relationship and relative permeability parameters assigned for the Brooks and Corey model considered in our electrolyte wetting simulation models. The pore-size distribution index is assumed to represent the pore distribution in the electrodes.

### 2.3. Software and Hardware Details

The wetting model was implemented by using COMSOL's "Porous Media Flow" module, which solves physical equations to describe a multiphase flow in a porous medium. Within this module, the biphasic flow of electrolyte and air was defined by adding the "Multiphase Flow in Porous Media" interface, which includes Darcy's law along with the physics to study phase transport in porous media. Darcy's law solves for the pressure in the stacked porous domains, and the phase transport physics solves for the electrolyte and air phases in the electrolyte and air (two-phase) mixture inside the porous electrodes and separator. A time-dependent study has been added to the model to determine how the dependent variables change with time. A single study step in COMSOL "Model Builder" is used to solve the problem using the time-dependent PARDISO solver for the 2D and 3D models. The time-dependent step first compiles all the equations to solve the problem via a linear Lagrange geometry shape function. Then, it only solves the pressures and phase saturations of

Darcy's law and Phase Transport in the "Porous Media interface" in the software. Output is recorded every 100 s during the calculation, and the simulation stops once it has fulfilled a set condition or reached the stop time. For the final model, the stop time is set to 2 h after the parameter optimization tests were carried out. The dependent variables are scaled using an initial value setting. In this way, we can obtain accurate solutions and limit ill-conditioned matrices, which may cause numerical failures or slow the time to reach an accurate solution. More details about the software are given in Table S1, Supporting Information.

The hardware used to run the models is shared between two platforms. The first is a Dell Latitude 5520, with an Intel 11th Gen Intel core i7-1165G7 processor with 4 cores, 8 logical processors, and 16 GB of RAM memory, which is used to set up the models, perform short calculations, and run tests. The second is a cloud platform, equipped with an Intel Xeon CPU E5-2680 v4 with 28 cores and 500 GB of RAM memory hosted on MatriCS (UPJV's shared server platform), which is used to perform the most demanding calculations. Typical calculation times range from a few minutes for the 2D model to several hours for the 3D model.

## 3. Results and Discussion

### 3.1. 2D Model Results

The simulation of the 2D model was performed using the resources described in Section 2. For the parameters, boundary and initial conditions, Table 3–6 were considered. With these specifications, the infiltration process of the cell was simulated for 1 h and 6 min of virtual time, in 2 min of wall time. It was observed that the electrolyte infiltrated both electrodes and separator due to the pressure differences in the macroscopic porous domains. The saturations of the electrolyte and air phases as a function of time are shown in **Figure 4a**. It can be observed that as the electrolyte infiltrates the cell, the air phase decreases and reaches a plateau after  $\approx 1$  h. The opposite trend is observed for the electrolyte phase. The final saturation values reach 0.9 and 0.1 for the electrolyte and air phases, respectively. This indicates that the system has reached equilibrium, and the simulated process is complete.

The calculated wetting dynamics of each component of the porous cell are plotted in Figure 4b. First, the positive and the negative electrodes have similar electrolyte saturation curves with a final plateau value of about 90%, while for the separator, this saturation value is slightly lower (85%) and has a different filling trend. The separator filling rate exceeds that observed for the other two electrodes during the first part of the process. This can be seen from the initial times in Figure 4c, where the first derivative of the saturation shows a higher initial value for the separator compared to the electrode ones. However, after 10 min, the wetting rate of the separator slowly decreases. This cell wetting behavior is in agreement with previous literature reports,<sup>[5]</sup> and it can be attributed to the higher porosity of the separator. In the case of the electrodes, we observe that the wetting process takes a longer time to start, then it accelerates

**Table 6.** Input parameters for Brooks and Corey models.

Parameters	Symbol	Value
Entry pressure [kPa]	$P_e$	800
Pore-size distribution index	$\lambda$	2.7 (separator), 2 (electrodes)
Residual saturation	$S_{re}, S_{ra}$	0
Relative permeability exponent (electrolyte)	$K_{re}$	$(2 + 3\lambda)/\lambda$
Relative permeability exponent (air)	$K_{ra}$	$(2 + 3\lambda)/\lambda$

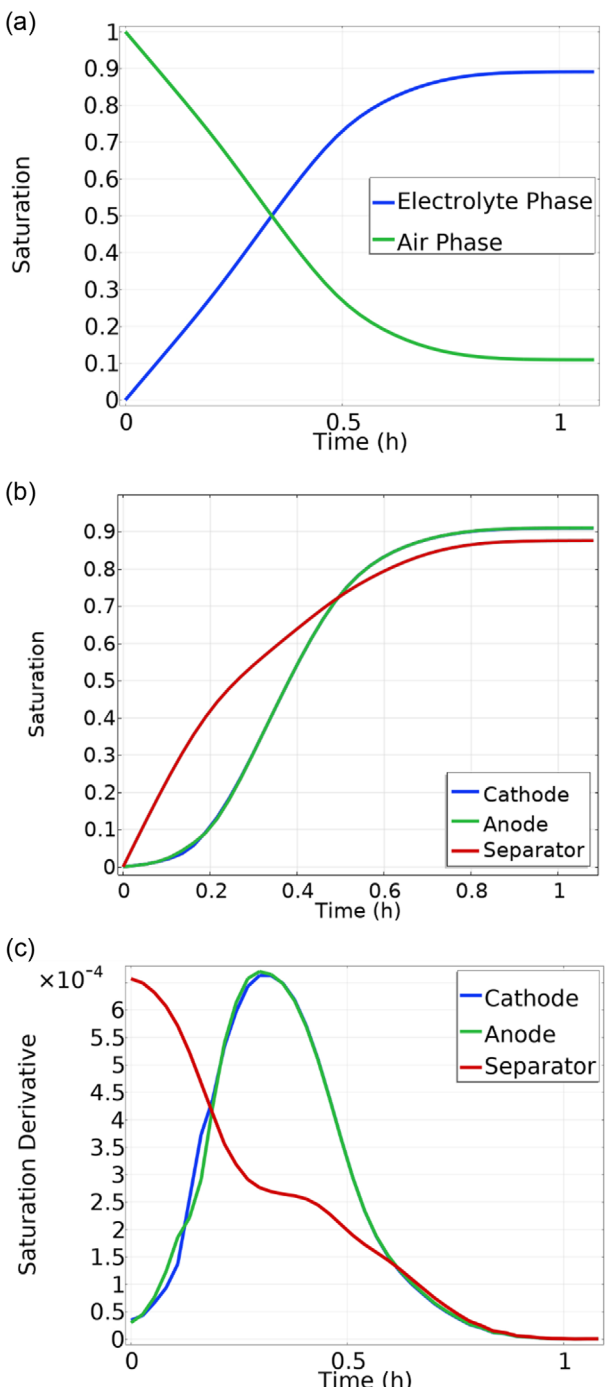


**Figure 4.** Comparison of total phase and components saturations in the 2D model a) phase saturations of air (green curve) and electrolyte (blue curve) in the 2D model cell, b) component saturations (graphite anode -green curve-, NMC111 cathode -blue curve-, and separator -red curve-) in the 2D model, and c) first derivative of the saturation profiles of electrolyte in the electrodes and in the separator as a function of time.

up to a maximum value around 20 min, and finally, it slowly decreases. In terms of wetting rates, the Graphite electrode is slightly faster than the NMC111 electrode (Figure 4c), which can also be explained by the larger porosity and mean pore size values extracted from literature. The saturation degree is also

highly dependent on the entry capillary pressure. This is clearly shown in Figure S1 of the Supporting Information, where increasing entry capillary pressure considerably decreases the electrolyte saturation degree.

To closely follow the 2D evolution of the saturation on the cell geometry, Figure 5 shows snapshots of the electrolyte wetting process at different time steps. Figure 5a displays the porous media into which the electrolyte flows in (anode, cathode, and separator), while the current collectors are represented as blank spaces between each layer (composed of electrodes and separator). The electrolyte saturation in the cell increases faster in the first snapshots and then stabilizes at a high value of 0.9 in the last snapshots. Also, the contour plot video in the Supporting Information (Video S1) shows that all the domains are saturated with electrolyte to different degrees, since the electrodes and the separators have different properties (pore size, porosity, and permeability).

The optimized parameters used in the 2D model were transferred to the miniature 3D cell to test the feasibility before running the full 3D cell. To determine if a reduced-order consideration of the cell geometry as concentric instead of spiral is a good enough representation of the system, we compare the results obtained by running the miniature 3D cell model with both concentric and spiral geometries. The result shown in Figure 6 demonstrates that the miniature 3D cell (now hereafter denoted as miniature 3D spiral cell for this comparison) wetting dynamics is qualitatively similar to the one displayed by a 3D miniature cell generated from performing a revolution along the z-axis of the 2D model cell (which is a concentric model).

Nevertheless, wetting proceeds faster in the spiral geometry than in the concentric cell (Figure 6a). This can be attributed to the consideration of the electrodes and separator to be filled as continuous layers. While for the concentric cell, the wetting rate is decreased due to the discontinuous filling of the individual layers of electrodes and separator. The total wetting degree for the spiral geometry reaches a wetting plateau at 0.92 in 40 min, while for the concentric cell the plateau is reached at 0.9 and in 1 h. The same behavior can be seen for the individual electrodes and separator (Figure 6b). This result demonstrates that the spiral jelly roll geometry influences the wetting rate and saturation degree. Then, a hypothetical concentric cell is not a good approximation since it is not able to fully capture the wetting behavior of the real cell geometry.

### 3.2. 3D Full-Height Cell Model Results

We study the electrolyte wetting dynamics of the cylindrical 18650 format cell using the full-height 3D cell with the spiral jelly roll. It is worth reminding that the simulated jelly roll consists of 21 windings with repeating layers, the flattened jelly roll contains the separator, a double-sided anode, another separator, and finally a double-sided cathode. The 21-layer configuration correspond to the typical number of layers found in commercial 18650 formats cells. Therefore, the actual cell geometry is well-represented in the model. The model is informed using the data

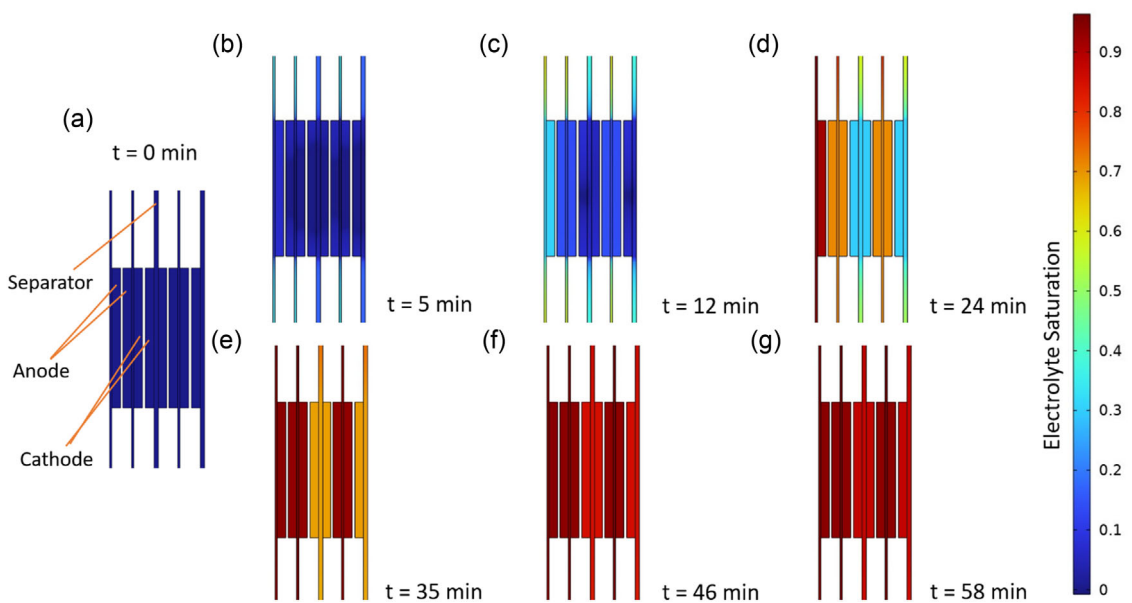


**Figure 5.** Contour plots of the 2D model showing the electrolyte wetting saturation in the a) initial condition and at b) 5 min, c) 12 min, d) 24 min, e) 35 min, f) 46 min, and g) 58 min of the virtual wetting time. It should be noted that the current collectors are not shown because there is no electrolyte flow in them. The current collectors are placed between two adjacent cathodes and between two adjacent anodes. The color bar on the right indicates the volume fraction of the electrolyte saturation.

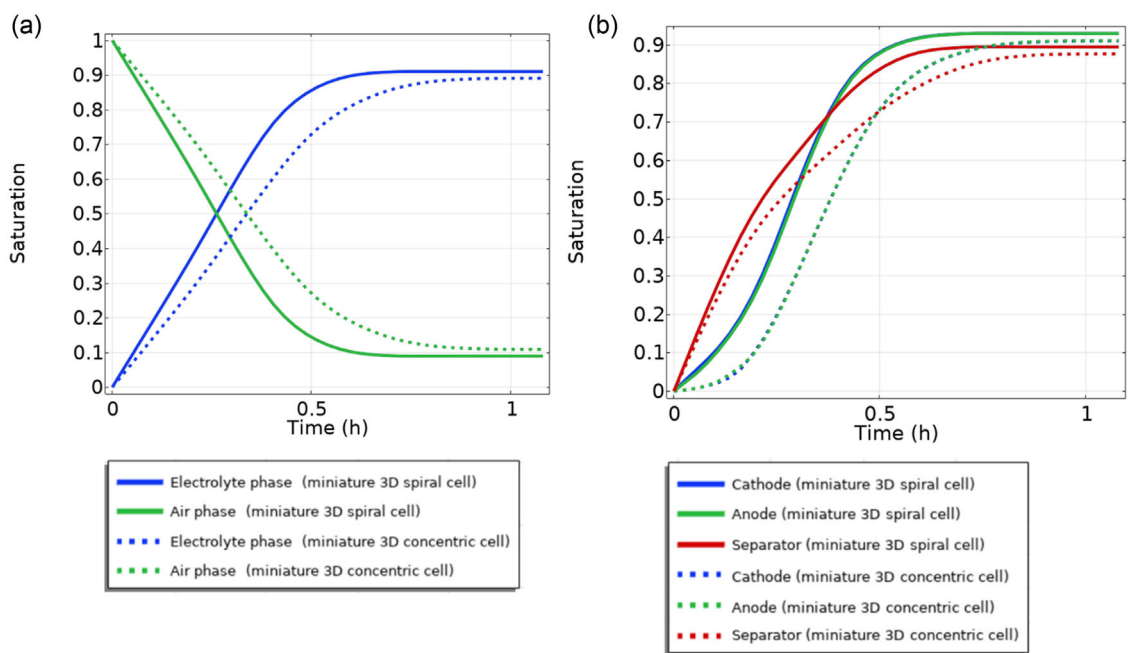


**Figure 6.** Miniature 3D spiral (solid lines) and concentric (dashed lines) cells saturation degree, a) electrolyte and air phase saturation, and b) saturation profiles of electrolyte in the electrodes and in the separator as a function of time.

extracted from the literature. Considering the same mass flux and injection pressure, the difference in height means that the flux gradually reduces to zero as the total pressure drop decreases. Therefore, further parameter optimization for the capillary pressures is performed by using a parametric study to determine an optimal value. The optimal value for which wetting is maximized

for the given set of inputs, was found to be 40 kPa. Due to the increase in computational complexity and the increase in mesh elements, this calculation took 11 h of wall time to simulate the virtual electrolyte soaking dynamics to reach the final saturation values. The total electrolyte saturation curves as a function of time are plotted in Figure 7a, showing the saturation of the

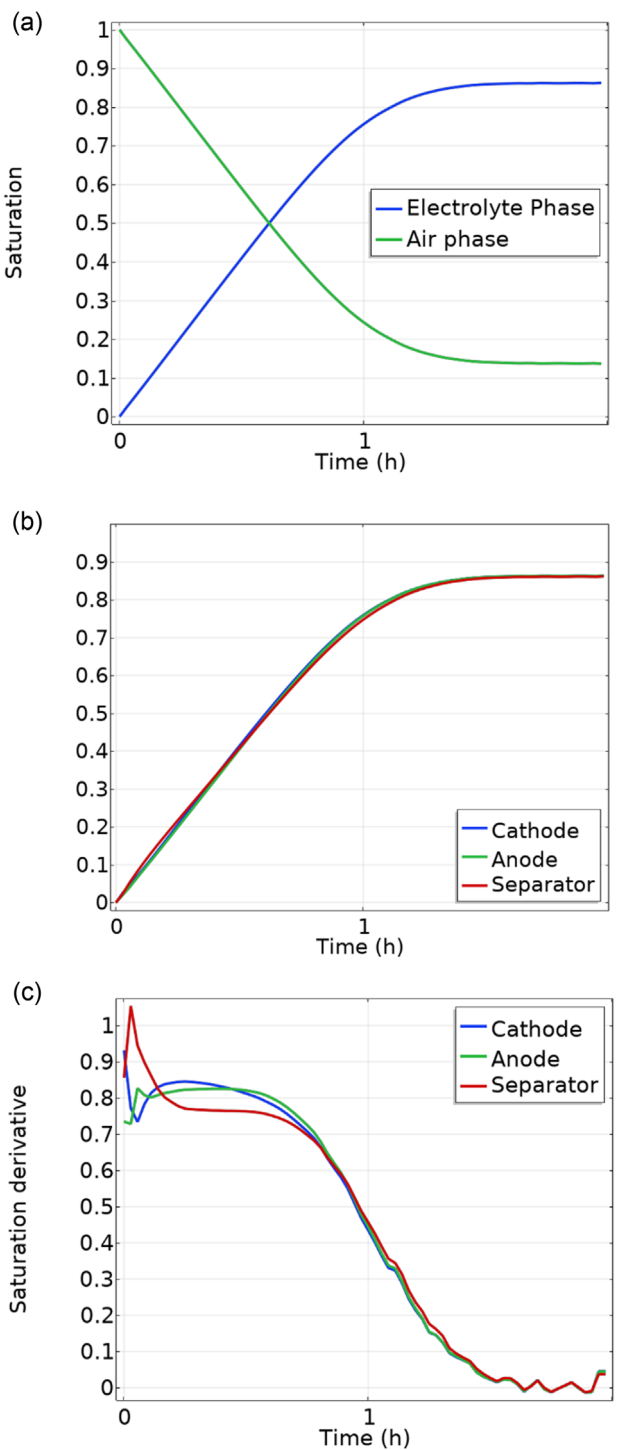


**Figure 7.** Comparison of total phase and component saturations in the 3D spiral model a) phase saturations of air (green curve) and electrolyte (blue curve) over the cell stack, b) component saturations (graphite anode -green curve-, NMC111 cathode -blue curve-, and separator -red curve-), and c) first derivative of the saturation profiles of electrolyte in the electrodes and in the separator as a function of time, all computed by using our full-height 3D spiral model.

electrolyte and air phases over 2 h. At the end, the electrolyte saturation curve reaches a plateau with an average saturation of 86%.

The individual saturation curves for the 3D cell components are shown in Figure 7b, consistent with the overall average phase saturation. Initially, the wetting of the separator reached a higher rate, when compared to both anode and cathode, but it is equilibrated with them as wetting progressed. Finally, the separator has a slightly lower degree of saturation than either electrode. The initial bump in the separator saturation derivative curve is due to the faster initial wetting in Figure 7c. The positive and negative components both had similar saturation profile. The difference in saturation curves between the full-height cell and the miniature cell model is attributed to the extended wetting initiation points in the full-height cell, and also due to the starting entry capillary pressure. At the start of the simulation, a larger volume of electrolyte enters both the separator and electrodes, resulting in more uniform saturation profiles as the simulation progresses. Although the model does not capture microstructural variations in saturation, it successfully predicts the overall saturation trends. The Graphite electrode filled faster due to its larger average pore size, while the NMC111 electrode has a slightly higher electrolyte saturation degree. Additionally, in Figure 7c, the derivative of the saturation decreases in the first few minutes for the cathode before increasing, and the plateau is higher than for the anode. The reason for this can be explained by the nature of the wetting, which starts with the saturation of the first outer layer of the separator first, before the saturation progresses inwards towards the electrodes. Also, the fluctuations observed at the end of the derivative curves are due to slightly varying saturation speeds at the end of the simulated wetting process. At the end, the NMC111 electrode had the highest degree of saturation, in accordance with the profiles reported in the literature with LBM models.<sup>[9]</sup> It should be noted that this comparison is not directly equivalent, as in these previous works,<sup>[9]</sup> the modeling was performed at the mesoscale. Nevertheless, we found that the wetting speed is governed primarily by capillary pressure and pore permeability.

Figure 8 shows the level of electrolyte saturation at different time frames during the electrolyte wetting process in the jelly roll components for the full-height 3D spiral cell geometry. These time frames start from the initial conditions (Figure 8a) and end when the wetting process is finalized (Figure 8g). After 20 min of wetting (Figure 8b), the cell has reached approximately a 25% of electrolyte saturation. However, we can still observe some localized increase of electrolyte saturation, in the zones highlighted in Figure 8h (outer separator layer and bottom fringes of jelly roll). From 20 to 80 min of simulated time, a gradual electrolyte wetting is observed (Figure 8c-e). However, a slower penetration of the electrolyte into the porous components is observed around 100 min (Figure 8f), to finally reach the maximum saturation at 2 h. At the end of the simulation, there are still some unfilled pores in the electrodes, especially residual air phase remains heterogeneously distributed near the bottom of the cell (Figure 8i). The dynamic evolution is also reported in Video S2 of the Supporting Information, where the gradual infiltration of the electrolyte into the cell can be tracked, and the differences in the wetting dynamics of the cell are highlighted.

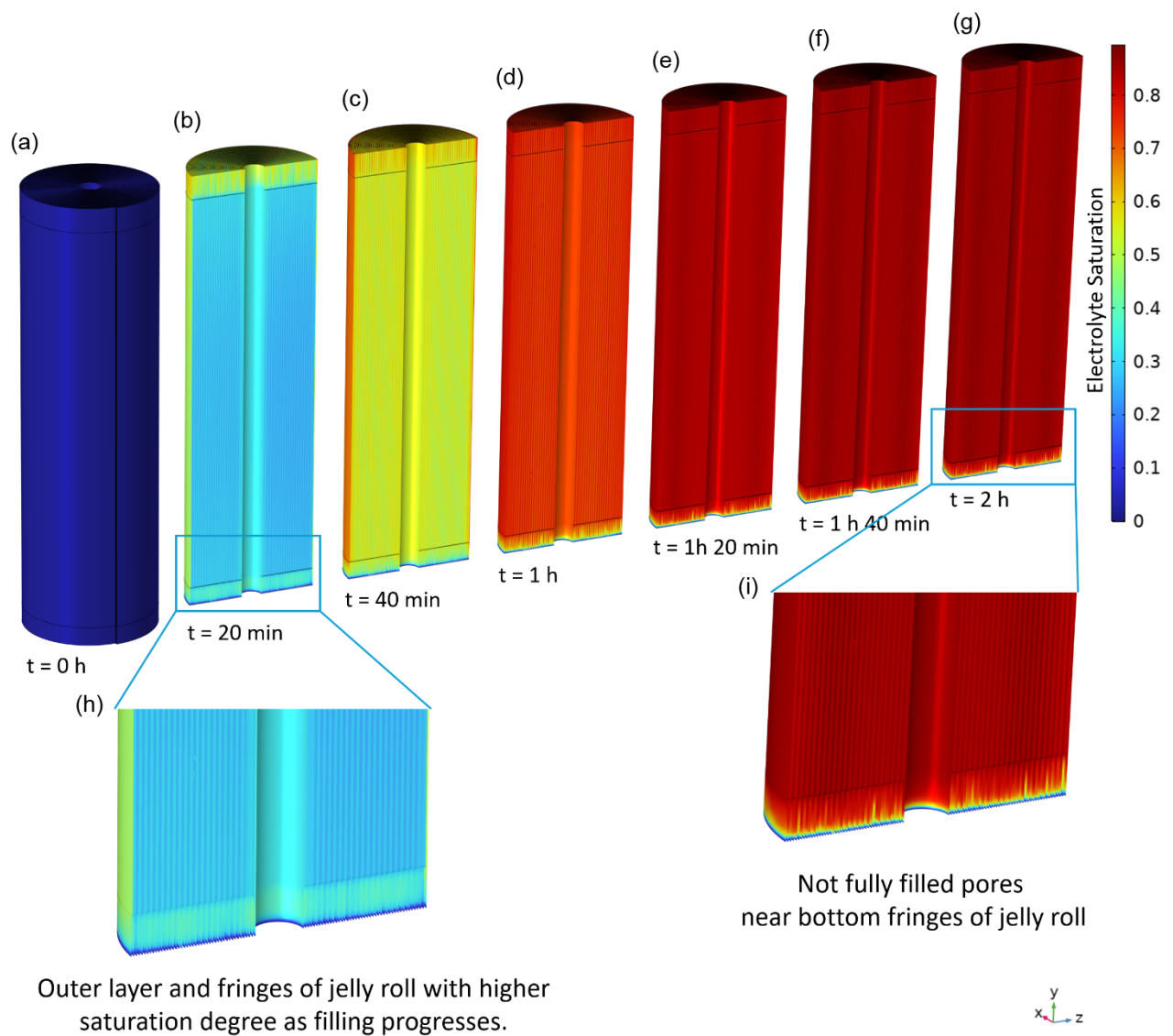


**Figure 8.** Contour plots of the 3D model with the electrolyte simulation process showing the electrolyte saturation in the a) initial condition and after b) 20 min, c) 40 min, d) 1 h, e) 1 h 20 min f) 1 h 40 min, and g) 2 h. The color bar on the right indicates the volume fraction of the electrolyte saturation. Snapshot at the bottom of the cell h) at 20 min, and i) at 2 h.

#### 4. Conclusions

In this study, we presented the development of novel engineering-oriented 2D and 3D continuum models to simulate the electrolyte wetting process in cylindrical cells with the 18650 format. To the best of our knowledge, this is the first computational model of its kind, specifically targeting the simulation of the wetting of this cell format and at the macroscopic scale. To fulfill this objective, volume-averaged properties were used for simulating wetting in each successive layer of the jelly roll. We have replicated electrolyte infiltration to study its behavior and provide a computational tool that can support the optimization of the electrolyte wetting step in battery cell manufacturing. We consider the configuration of the jelly roll and model parameters from literature to calibrate and validate the model simulations.

The cell geometry was designed using SolidWorks, and the model parameters reflect the case of an NMC111-Graphite LIB cell. A pressure-saturation mathematical framework has been derived, yielding the equations that needs to be numerically solved in order to provide the evolution of phase pressures and saturations during wetting. The equations governing the two-phase flows through the pore network of the electrodes and the separator were successfully implemented in COMSOL Multiphysics, where numerical solutions were obtained through the FEM approach. The modeling approach was carried out through two levels of complexity: an initial reduced-order 2D model to study coupled physics and perform parameter sensitivity analysis, followed by a full-scale 3D model representing the entire cell with the spiral geometry. This hierarchical strategy allowed us to investigate how the physical properties of the cell,

including its size and complex shape, influence the electrolyte wetting dynamics. Key figures of merit such as wetting speed, saturation heterogeneity, and overall saturation degree were discussed.

The observed wetting process in the full-scale model was primarily driven by the jelly roll architecture and capillary pressure. First, a higher wetting speed in the outer layers, followed by gradual impregnation from the top and bottom, and the center being the last region to be wetted. This is similar to the behavior observed in pouch cells. After 2 h of simulated wetting, with an input electrolyte pressure of 800 kPa and an entry capillary pressure of 40 kPa for the 3D 18650 cell, the electrolyte saturation plateaued at 86%. At this plateau, electrolyte saturation is relatively homogeneously distributed throughout the entire cell. Regarding gas entrainment, the findings of our model are in agreement with experimental observations on the outer windings of a 21700 cylindrical cell.<sup>[35]</sup> Our model allows visualizing, with unprecedented details, the processes happening in the inner windings of the jelly roll, something very challenging to achieve by state-of-the-art experimental techniques. This work advances the understanding of the electrolyte wetting process in LIB manufacturing. It also provides critical insights into the dynamics of electrolyte wetting in 18650 cell formats. The herein obtained results agree with experimental results previously reported in the literature. To further improve the predictions of our model, calibration and validation could be performed by using neutron or X-ray imaging techniques. These could allow us to track the electrolyte volume fraction (saturation) evolution in real-time during the filling and pre-aging stage.

In addition, this model can be used in the future to explore additional wetting steps and conditions to reach higher saturation degrees, analyze different cylindrical cell configurations (e.g., with different electrode porosities and thicknesses) and cell formats, as well as evaluating different AM and electrolyte chemistries. As another perspective, this macroscale model for the electrolyte wetting could be coupled with a mesoscale one within a multiscale modeling workflow. This could be done, for example, by parameterizing the model developed in this work with properties calculated with our previously reported LBM model.<sup>[9]</sup> The model could be used as a building block to create a digital twin of the electrolyte wetting step, allowing real-time optimization of parameters to increase electrolyte saturation and homogeneous electrolyte distribution throughout the cell. Additionally, a machine learning (ML) surrogate model could be trained on a dataset generated with this model to reduce the computational cost (like our previously reported ML models trained on LBM electrolyte infiltration simulation data<sup>[19,46]</sup>). Also, as a perspective, the analysis of the influence on the electrolyte wetting of different electrode manufacturing parameters applied on previous steps could be addressed. Ultimately, the work presented here provides a detailed and descriptive framework for physics-based 3D-resolved modeling at the macroscale that could be coupled with our manufacturing pipeline modeling tools to build predictive digital models that can be used in optimization loops to find the optimal manufacturing parameters.<sup>[30]</sup>

## Acknowledgements

A.A.F. and I.C.-S. acknowledge funding from the French National Research Agency (ANR) on the context of the "France 2030 program" and the Priority Research Programs and Equipment (PEPR) "Batteries" (grant ANR-22-PEBA-0002, Project BATMAN). A.A.F. and F.F. acknowledge financial support from the EU Horizon Europe project DigiCell (grant agreement no. 101135486). A.A.F. and E.Y. acknowledge the M.Sc. programme MESC+ (Materials for Energy Storage and Conversion) for the support. The authors also acknowledge the MatriCS HPC platform from Université de Picardie Jules Verne for the support and for hosting the nodes used for the calculations reported in this manuscript. A.A.F. acknowledges Institut Universitaire de France for the support.

## Conflict of Interest

The authors declare no conflict of interest.

## Author Contributions

**Emmanuel Yerumoh:** writing—original draft; visualization; software; methodology; investigation; formal analysis; and conceptualization. **Imelda Cardenas-Sierra:** writing—review & editing; visualization; software; methodology; and conceptualization. **Francisco Fernandez:** writing—review and editing; visualization; methodology; and conceptualization. **Alejandro A. Franco:** conceptualization; methodology; writing—review and editing; supervision; resources; project administration; and funding acquisition.

## Data Availability Statement

The data that support the findings of this study are available from the corresponding author upon reasonable request.

**Keywords:** electrolyte wetting · finite element method · jelly roll · lithium ion batteries

- [1] Y. S. Duh, Y. Sun, X. Lin, J. Zheng, M. Wang, Y. Wang, X. Lin, X. Jiang, Z. Zheng, S. Zheng, G. Yu, *J. Energy Storage* **2021**, *41*, 102888.
- [2] C. P. Grey, D. S. Hall, *Nat. Commun.* **2020**, *11*, 6279.
- [3] M. Armand, P. Axmann, D. Bresser, M. Copley, K. Edström, C. Ekberg, D. Guyomard, B. Lestriez, P. Novák, M. Petranikova, W. Porcher, S. Trabesinger, M. Wohlfahrt-Mehrens, H. Zhang, *J. Power Sources* **2020**, *479*, 228708.
- [4] F. M. Zanotto, D. Z. Dominguez, E. Ayerbe, I. Boyano, C. Burmeister, M. Duquesnoy, M. Eisentraeger, J. F. Montaño, A. Gallo-Bueno, L. Gold, F. Hall, N. Kaden, B. Muerkens, L. Otaegui, Y. Reynier, S. Stier, M. Thomitzek, A. Turetsky, N. Vallin, J. Wessel, X. Xu, J. Abbasov, A. A. Franco, *Batteries Supercaps* **2022**, *5*, e202200224.
- [5] D. H. Jeon, *Energy Storage Mater.* **2019**, *18*, 139.
- [6] F. J. Günter, J. Keilhofer, C. Rauch, S. Rössler, M. Schulz, W. Braunwarth, R. Gilles, R. Daub, G. Reinhart, *J. Power Sources* **2022**, *517*, 230668.
- [7] J. Jagemeister, F. J. Günter, T. Rinner, F. Zhu, A. Papst, R. Daub, *Batteries* **2022**, *8*, 159.

- [8] J. Wanner, K. P. Birke, *Batteries* **2022**, *8*, 277.
- [9] A. Shodiev, E. Primo, O. Arcelus, M. Chouchane, M. Osenberg, A. Hilger, I. Manke, J. Li, A. A. Franco, *Energy Storage Mater.* **2021**, *38*, 80.
- [10] A. Shodiev, F. M. Zanotto, J. Yu, M. Chouchane, J. Li, A. A. Franco, *Energy Storage Mater.* **2022**, *49*, 268.
- [11] R. Korthauer, *Lithium-Ion Batteries: Basics and Applications*, Springer-Verlag GmbH DE, Berlin **2018**.
- [12] S. Michaelis, J. Schütrumpf, A. Kampker, H. Heimes, B. Dorn, S. Wennemar, A. Scheibe, S. Wolf, M. Smulka, B. Ingendoh, A. Thielmann, C. Neef, T. Wicke, L. Weymann, T. Hettesheimer, A. Kwade, L. Gottschalk, C. von Boeselager, S. Blömeke, A. Diener, M.-W. von Horstig, J. Husmann, M. Kouli, M. Mund, G. Ventura Silva, M. Weber, M. Podbreznik, A. Schmetz, *Roadmap Battery Production Equipment 2030. Update 2023*, VDMA Verlag, Frankfurt **2023**.
- [13] C. Sauter, R. Zahn, V. Wood, *J. Electrochem. Soc.* **2020**, *167*, 100546.
- [14] M. P. Lautenschlaeger, B. Prifling, B. Kellers, J. Weinmiller, T. Danner, V. Schmidt, A. Latz, *Batteries Supercaps* **2022**, *5*, e202200090.
- [15] M. Abubaker, C. H. Sohn, H. M. Ali, *J. Therm. Anal. Calorim.* **2024**, *149*, 5443.
- [16] F. Chen, T. Chen, Z. Wu, Z. Zhou, J. Su, Y. Zheng, X. Han, in *Proc. of 2024 IEEE 7th Int. Electrical and Energy Conf., CIEEC 2024*, Institute of Electrical and Electronics Engineers Inc., Harbin, China **2024**, pp. 3457–3464.
- [17] A. C. Ngandjong, T. Lombardo, E. N. Primo, M. Chouchane, A. Shodiev, O. Arcelus, A. A. Franco, *J. Power Sources* **2021**, *485*, 229320.
- [18] E. N. Primo, M. Chouchane, M. Touzin, P. Vazquez, A. A. Franco, *J. Power Sources* **2021**, *488*, 229361.
- [19] A. El Malki, M. Asch, O. Arcelus, A. Shodiev, J. Yu, A. A. Franco, *J. Power Sources Adv.* **2023**, *20*, 100114.
- [20] A. Davoodabadi, J. Li, H. Zhou, D. L. Wood, T. J. Singler, C. Jin, *J. Energy Storage* **2019**, *26*, 101034.
- [21] T. Knoche, V. Zinth, M. Schulz, J. Schnell, R. Gilles, G. Reinhart, *J. Power Sources* **2016**, *331*, 267.
- [22] A. Schilling, S. Wiemers-Meyer, V. Winkler, S. Nowak, B. Hoppe, H. H. Heimes, K. Dröder, M. Winter, *Energy Technol.* **2019**, *8*, 1900078.
- [23] M. Dent, S. Grabe, C. Lekakou, *Batteries Supercaps* **2024**, *7*, e202300327.
- [24] *Processing and Manufacturing of Electrodes for Lithium-Ion Batteries* (Eds: J. Li, C. Jin), Institution of Engineering and Technology, London **2023**.
- [25] Y. Xie, H. Zou, H. Xiang, R. Xia, D. Liang, P. Shi, S. Dai, H. Wang, *J. Membr. Sci.* **2016**, *503*, 25.
- [26] H. Cui, D. Ren, M. Yi, S. Hou, K. Yang, H. Liang, X. Feng, X. Han, Y. Song, L. Wang, X. He, *Nano Energy* **2022**, *104*, 107874.
- [27] J. B. Habedank, F. J. Günter, N. Billot, R. Gilles, T. Neuwirth, G. Reinhart, M. F. Zaeh, *Int. J. Adv. Manuf. Technol.* **2019**, *102*, 2769.
- [28] S. G. Lee, D. H. Jeon, *J. Power Sources* **2014**, *265*, 363.
- [29] F. J. Günter, S. Rössler, M. Schulz, W. Braunwarth, R. Gilles, G. Reinhart, *Energy Technol.* **2019**, *8*, 1801108.
- [30] J. F. Troncoso, F. M. Zanotto, D. E. Galvez-Aranda, D. Z. Dominguez, L. Denisart, A. A. Franco, *Batteries Supercaps* **2024**, *8*, e202400385.
- [31] J. Xu, A. C. Ngandjong, C. Liu, F. M. Zanotto, O. Arcelus, A. Demortière, A. A. Franco, *J. Power Sources* **2023**, *554*, 232294.
- [32] T. Lombardo, F. Caro, A. C. Ngandjong, J. B. Hoock, M. Duquesnoy, J. C. Delepine, A. Ponchelet, S. Doison, A. A. Franco, *Batteries Supercaps* **2022**, *5*, e202100324.
- [33] D. E. Galvez-Aranda, T. Le Dinh, U. Vijay, F. M. Zanotto, A. A. Franco, *Adv. Energy Mater.* **2024**, *14*, 2400376.
- [34] S. K. Mohammadian, Y. Zhang, *Int. J. Heat Mass Transf.* **2018**, *118*, 911.
- [35] J. Wanner, M. Burgard, N. Othman, S. Singh, K. P. Birke, *Batteries Supercaps* **2025**, *8*, e202400531.
- [36] J. Hagemeister, A. Elkoshet, A. Yakici, F. Günter, Y. Hu, R. Daub, *Energy Technol.* **2024**, *13*, 2401708.
- [37] COMSOL - Software for Multiphysics Simulation, <https://www.comsol.com/> (accessed: 2024).
- [38] The Proven Solution for 3D Design and Product Development | SOLIDWORKS, <https://www.solidworks.com/> (accessed: 2024).
- [39] T. Waldmann, R. G. Scurtu, K. Richter, M. Wohlfahrt-Mehrens, *J. Power Sources* **2020**, *472*, 228614.
- [40] W. Sheng, *Eur. J. Mech., B* **2020**, *80*, 60.
- [41] M. J. Blunt, *Multiphase Flow in Permeable Media*, Cambridge University Press, Cambridge **2017**, pp. 219.
- [42] P. Binning, M. A. Celia, *Adv. Water Resour.* **1999**, *22*, 461.
- [43] J. Wanner, K. P. Birke, *J. Energy Storage* **2024**, *87*, 111410.
- [44] C. S. Stefan, D. Lemordant, B. Claude-Montigny, D. Violleau, *J. Power Sources* **2009**, *189*, 1174.
- [45] S. G. Lee, D. H. Jeon, B. M. Kim, J. H. Kang, C.-J. Kim, *J. Electrochem. Soc.* **2013**, *160*, H258.
- [46] A. Shodiev, M. Duquesnoy, O. Arcelus, M. Chouchane, J. Li, A. A. Franco, *J. Power Sources* **2021**, *511*, 280384.
- [47] B. Reschke, US8047241B2 **2011**.

Manuscript received: June 3, 2025

Revised manuscript received: July 10, 2025

Version of record online: